Title

Interface Engineering of Carrier-Protein-Dependent Metabolic Pathways

Journal

ACS Chemical Biology, 18(9)

ISSN

1554-8929

Authors

Sztain, Terra

Corpuz, Joshua C

Bartholow, Thomas G

et al.

Publication Date

2023-09-15

DOI

10.1021/acschembio.3c00238

Peer reviewed

Published in final edited form as:

ACS Chem Biol. 2023 September 15; 18(9): 2014–2022. doi:10.1021/acschembio.3c00238.

Interface Engineering of Carrier Protein–Dependent Metabolic Pathways

Terra Sztain[†],

Joshua C. Corpuz[†],

Thomas G. Bartholow,

Javier O. Sanlley Hernandez,

Ziran Jiang,

Desirae A. Mellor,

Graham W. Heberlig,

James J. La Clair,

J. Andrew McCammon,

Michael D. Burkart[*]

Department of Chemistry and Biochemistry, University of California, San Diego, 9500 Gilman Drive, La Jolla, California 92093, United States

Abstract

Carrier protein dependent metabolic pathways biosynthesize fatty acids, polyketides, and non–ribosomal peptides, producing metabolites with important pharmaceutical, environmental, and industrial properties. Recent findings demonstrate that these pathways rely on selective communication mechanisms involving protein–protein interactions (PPIs) that guide enzyme reactivity and timing. While rational design of these PPIs could enable pathway design and modification, this goal remains a challenge due to the complex nature of protein interfaces. Computational methods offer an encouraging avenue, though many score functions fail to predict experimental observables, leading to low success rates. Here, we improve upon the Rosetta score function, leveraging experimental data through iterative rounds of computational prediction and mutagenesis, to design a hybrid fatty acid–non–ribosomal peptide initiation pathway. By increasing the weight of the electrostatic score term, the computational protocol proved more predictive, requiring fewer rounds of iteration to identify mutants with high in vitro activity. This

[*]**Corresponding Authors** Michael D. Burkart – Department of Chemistry and Biochemistry, University of California, San Diego, 9500 Gilman Drive, La Jolla, California 92093, United States; mburkart@ucsd.edu.

[†]Author Contributions

T. Sztain and J. C. Corpuz contributed equally. T.S. designed and performed the computational interface design. J.C.C. carried out the cloning, purification, enzyme assays, and structural analysis. T.G.B., J.S.H., and D.A.M. prepared and performed the NMR titrations. J.J.L performed cellular extractions and NMR analysis. G.W.H. performed chemical probe synthesis. Z.J. and J.J.L. contributed to data analyses and synthetic effort that was not included within the manuscript. T.S., J.C.C., J.J.L. and M.D.B. contributed to planning, writing, and editing of the manuscript.

Supporting Information

Supporting Information is available free of charge at https://pubs.acs.org/doi/10.1021/. All design scripts are available at https://github.com/tsztain/PltF–AcpP–design.

• Figures S1-S7 and Tables S1-S4; and copies of NMR spectra on the synthetic intermediates and chemical probes.

The authors declare no competing interests.

allowed efficient design of new PPIs between a non–ribosomal peptide synthetase adenylation domain, PltF, and a fatty acid synthase acyl carrier protein, AcpP, as validated by activity and structural studies. This method provides a promising platform for customized pathway design, establishing a standard for carrier protein dependent pathway engineering through PPI optimization.

Graphical Abstract

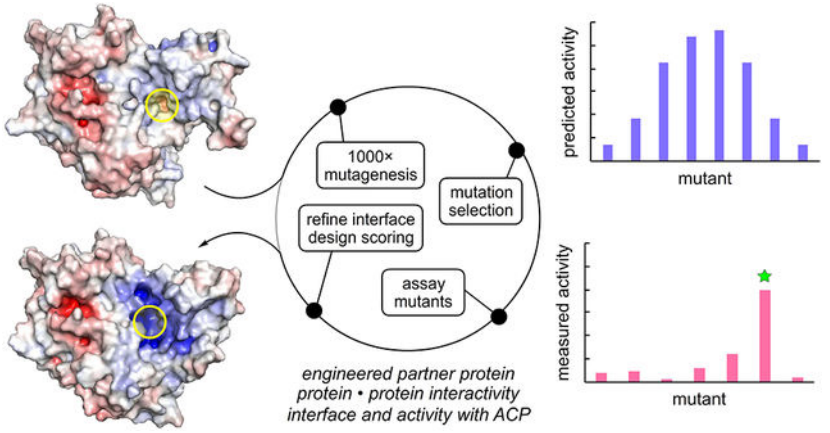

INTRODUCTION

The ability to design and evolve catalysis between unrelated primary and secondary metabolic players remains a long–elusive goal for the carrier protein dependent pathways that include fatty acid synthase (FAS), polyketide synthase (PKS), and non–ribosomal peptide synthetase (NRPS). Although not broadly appreciated until recently, protein–protein interactions (PPIs) have been demonstrated to be responsible for enzyme selectivity and pathway organization in these carrier protein dependent pathways.[1] Within recent years, these PPIs have been structurally characterized in solution,[1,2] crystal structures,[3-8] and through microscopy;[9] predicted *in silico*;[2] abrogated by mutagenesis;[1] and improved by rational design.[10] What has remained uncharted, however, is the design of PPIs between non–reactive carrier protein–enzyme pairs for gain–of–function activity. The ability to rapidly engineer enzyme selectivity has the potential to revolutionize design and control these metabolic pathways. Here, we demonstrate development of a computational platform for evolving PPIs between carrier proteins and enzymes from previously incompatible pathways. We show how iterating computational docking and mutagenesis with experimental feedback can be leveraged to accelerate PPI engineering and demonstrate production of a functional unnatural product through a chimeric FAS–NRPS pathway construction.

In *Pseudomonas fluorescens*, the biosynthesis of the antibiotic, pyoluteorin, is initiated by the type II NRPS adenylation (A) domain, PltF, which activates and attaches L–proline to the thiol of the phosphopantetheine (PPant) of the peptidyl carrier protein (PCP), *holo*–PltL, *via* an ATP dependent mechanism (Figure 1A).[11] PltL transfers the prolyl group between tailoring domains for functionalization prior to transfer to a Type I PKS. Recent efforts were

able to deduce the PPIs between PltF and PltL through nuclear magnetic resonance (NMR) experiments and X–ray crystallography,[12,13] thus providing dynamic and high–resolution information of the PltL • PltF protein–protein interface, which can be used as a model to guide the design of new PPIs between A domains and non–cognate carrier proteins.

The acyl carrier protein (ACP), AcpP, from *Escherichia coli* fatty acid biosynthesis was identified as a promising non–cognate carrier protein in the design of a new PPI with PltF. The *E. coli* fatty acid biosynthesis is a well–studied primary metabolic pathway due to its relevance as a drug target and fuel precursor production.[14,15] AcpP is responsible for the shuttling of the thio–templated fatty acid chain to a variety of partner enzymes, which includes but is not limited to the ketosynthase for fatty acid chain extension and the ketoreductase (KR), dehydratase (DH), and enoyl reductase (ER) for reduction of the β–ketone fatty acid to a fully saturated fatty acid.[16] Upon reaching a certain fatty acid chain length, the acyl chain is transferred into the production of the lipid bilayer or into the biosynthesis of secondary metabolites.[17,18] AcpP's role in shuttling substrates through the FAS cycle is critical towards production of the fatty acid product, thus making it a target towards loading unnatural substrates for extension and creation of unnatural fatty acid products.[19]

The success in chain extension of a variety of substrates prompted the idea to modify AcpP with amino acids using an NRPS A domain, specifically with PltF. To do so, a productive interface between PltF and AcpP must be designed to allow prolylation of AcpP, which would enable biosynthesis of an unnatural ω–pyrrolidine fatty acid upon chain elongation of the prolyl–AcpP by the *E. coli* FAS (Figure 1B). These functionalized fatty acids may be utilized as polymer precursors or further functionalized as potential therapeutic candidates with scaffolds like lanneaquinol and anaephene B.[20-23]

In this study, a computational workflow was developed using Rosetta to design new protein–protein interactions using the PltL–PltF crystal structure as a starting structure. The AcpP structure was aligned to PltL to mimic a binding interaction for AcpP and PltF, then subsequent *in silco* mutagenesis provided a library of PltF mutants that were predicted to form an interface with AcpP. The library of PltF mutants was prepared using site directed mutagenesis and each mutant was assayed for prolylation activity with AcpP using an HPLC based assay and LCMS validation. After 3 rounds of iterative mutagenesis with Rosetta, the mutant with the highest activity *in vitro* achieved a 182–fold increase in turnover rate for AcpP prolylation compared to wild type (WT) PltF. Refining the default Rosetta score function using data from our experimental assay improved design success rate, including a design with 1690–fold increased turnover rate. Analysis of a model of this most active PltF mutant revealed the utilization of 3 positively charged residues that can electrostatically complement the negatively charged AcpP. Overall, our computational interface design methodology successfully identified evolved PltF mutants for activity with AcpP within a few rounds of iterative mutagenesis.

RESULTS AND DISCUSSION

Iterative computational and experimental design of PltF • AcpP interface.

Increasing evidence has demonstrated the role of protein–protein interactions (PPIs) for controlling substrate specificity in carrier protein dependent pathways.[1,9] We therefore sought to design a new PPI between the non–cognate pairs, PltF and AcpP, to facilitate a new activity for PltF by attaching proline to *holo*–AcpP. We leveraged information from the recently characterized, cognate PltF • PltL interface resolved by X–ray crystallography (PDB ID: 6O6E).[13] AcpP shares 27% sequence identity with PltL and aligns with 1.8 Å RMSD (Figure S1). To focus on gain–of–function and avoid deleterious pathway effects for downstream synthetic biology approaches, we chose to focus mutations to PltF rather than AcpP.

The RosettaScripts[24] of the Rosetta Software Suite was used to determine initial PltF mutations to form a more favorable PltF • AcpP interface, using a protocol that iterates through 1,000 cycles of docking, design, minimization, and scoring with the Rosetta Energy Function 2015 (REF15) score function[25] (Figure 2). Design focused on PltF residues within 8 Å of the AcpP interface, though PltF residues K402 and K486 were prevented from re–design due to importance for PltF catalysis in adenylation and thiolation half-reactions.[13] An additional bonus score was applied to favor native residues to avoid excess mutations. Six mutations significantly persisted throughout all cycles and were assayed for activity as point mutations in PltF (mPltF): L235A, S253A, M257Q, N436Y, Q438R, and K457I. Two mutants showed increased activity compared to the WT baseline of 5% conversion, with N436Y prolylating 8% of the AcpP, and Q438R prolylating 38% of *holo*–AcpP (Figure 3). The kinetics were also increased from a turnover of 0.0109 AcpP h^{-1} in the WT up to 0.264 AcpP h^{-1} in the Q438R mutant (Table S1, Figure S7).

Encouraged by these initial results, we tested whether combining these initial mutants would produce an additive or synergistic effect. Double and triple mutants did not show increased prolylation activity (Figure S2). Next, we tested whether subjecting single mutants through a subsequent round of *in silco* mutations would result in newer mutants with increased activity. Surprisingly, many new mutants identified by Rosetta were unique compared to the first round of mutagenesis (Table S2). All the second-round mutants identified for PltF N436Y showed decreased activity compared to the 8% single mutant (Figure 3A, Table S2). Three of the second–round mutants for Q438R showed similar or increased activity compared to the 38% single mutant (LCMS validation of loading of Q438R PltF provided in Fig. S6), with the Q438R K472R and Q438R D263H double mutants prolylating over 60% AcpP (Figure 3A, Table S2). A third round with each of these double mutants identified the triple mutant Q438R K472R D263N, which prolylated 83% of *holo*–AcpP with a catalytic turnover of 1.98 AcpP h^{-1}, a 182-fold improvement compared to WT (Figure 3A, Tables S1-S2, Figure S7).

Refinement of Rosetta score function for improved design.

Application of the *in silco* Rosetta PPI design protocol iterating with experimental feedback identified a triple mutant of PltF with significantly increased activity compared to WT.

However, many of the mutants did not show any activity and the sequence profile identified by Rosetta was not well correlated with mutant activity. Improvement of computational score functions to predict PPIs *in vitro* remains an ongoing challenge.[24,26] Therefore, we sought to refine the Rosetta score function, such that the PPI design protocol would be more predictive of desired activity. Examination of the individual score terms (Table S3) revealed that the electrostatic score was more predictive of activity than the interface score. AcpP is a negatively–charged protein, and many native partners have been found to contain a basic binding patch, so electrostatic interactions were anticipated to play an important role.[27]

Several electrostatic coefficient weights were tested with the design protocol for the WT PltF–AcpP interface. The standard weight for the electrostatic term is 0.875, but we found that increasing the weight to 1.500 gave the best prediction of *in vitro* activity (Table S3). We next repeated the iterative design protocol for 3 rounds and found a remarkable increase in successful mutant predictability (Figure 3). Many fewer false positives (predicted mutants with no *in vitro* activity) and greater true positive results were generated. By the third round, all designs prolylated over 30%, five prolylated over 70% and the best design, Q438R D263K A230R, prolylated 92% of *holo*–AcpP (Figure 3B). The best design exhibited a turnover of 18.5 AcpP h^{-1}, a remarkable 1690–fold improvement relative to the WT PltF • AcpP reaction. Although a large improvement, WT PltF has a turnover rate with its cognate PltL partner of about 4,000 PltL h^{-1}.[28]

AcpP is highly charged compared to the more hydrophobic interfaces found in many PKS/NRPS CPs. Designing an interface without as clear-cut complementarity as negative and positive charges may prove more difficult. However, our strategy is likely transferrable to protein-protein interactions dominated by other forces. The REF15 score function is decomposed into 18 weighted terms which may be modified depending on the system of interest, and regardless of the property, increasing the weight of the energy term which is most correlated with experimental results is likely to improve design success.

Features of the engineered PltF • AcpP interface.

The cognate PltF • PltL interface primarily depends on hydrophobic interactions. The X–ray crystal structure revealed minimal hydrogen bonding interactions at the interface, including the side chain amine of PltF K457 with PltL G38 main chain carbonyl.[13] Interestingly, the initial superposition of AcpP onto PltL and relaxation with the Rosetta score function revealed salt bridges between PltF R234, R404, and R458 with AcpP E57, D35, and E21, respectively (Figure 4A). The AcpP • PltF Q438R D263K A230R model reveals additional putative salt bridges between PltF Q438R and D263K with AcpP D38 and D56, respectively (Figure 4B). With the refined Rosetta score, three design rounds introduced three positively charged residues while replacing a negatively charged residue, which increased the positive electrostatic potential at the entrance to the PPant tunnel compared to the slightly positive interface of the WT PltF (Figure 4C-D, Figure S3). The PltF A230R mutation is in a position that can form a long–range electrostatic interaction with the PPant phosphate (Figure S4).[28] The 4’-phosphopantetheine moiety was not modeled during the Rosetta design. Therefore, the A230R mutation was likely predicted due to increasing the overall positive charge of the Pltf interface, creating a more favorable binding patch for

AcpP. Since the phosphate also contains negative partial charges, this is a likely mode of increased binding activity, as observed by modeling the phosphopantetheine moiety with the designed interface. Recent structural and sequence analysis of PCP–A domain complexes also revealed the conservation of an electrostatic interaction adjacent to the PltF A230R position, where A domains utilize a positively charged residue to bind the phosphate of the PPant arm.[29]

Here we aimed only to select for mutants with the ability to prolylate AcpP. Since ATP binding and adenylation active sites remain largely untouched during engineering, we assume the adenylation half-reaction rate is the same going from WT to mutant. Thus, the rate-limiting step remains binding of the non-cognate AcpP partner protein. During this step, the amino acid adenylate intermediate may potentially disassociate, and thus the A domain will need to repeat the adenylation reaction. This means that we must either select for mutants that bind the adenylate stronger or mutants that better bind the carrier protein to reduce ATP turnover. In this study we focused only on enhancing carrier protein binding, which would in turn increase efficiency of energy consumption.

NMR titrations to detect engineered PPIs.

To determine whether the engineered PltF exhibited increased functional PPI surface with AcpP, ^{15}N–HSQC titrations were performed on the complexes. To prevent enzyme turnover, AcpP was loaded with a desulfo–PPant mimic. This isostere, maintains the native structural and dynamic features of *holo*–AcpP, allowing observation of interactions with PltF with native substrate in solution. (Figure S5). WT PltF was compared to the Q438R D263K A230R PltF mutant (mPltF). The WT PltF showed very minor chemical shift perturbations (CSPs), as expected for a non-cognate binding pair, while the mPltF showed 10 residues with greater CSPs than the largest WT CSP. (Figure 5A-E). These residues, in descending order of CSP value: D38, I69, M44, A59, E53, L42, I72, G33, Q66, S27 and E60, span both the binding interface and hydrophobic pocket of AcpP (Figure 5F-G). The residue with the largest CSP in mPltF is D38, corresponding to a putative D-R salt bridge engineered between D38 and Q438R, the mutant which persisted in all engineering rounds (Figure 4B, Figure 5E). Native binding partners from Fatty acid biosynthesis titrated with AcpP have also perturbed the residues S27, D38, L42, M44, and Q66.[2] Residues S27, D38 and L42, have also been previously shown to play an important role in AcpP communication.[1] Residue D56 does not show significant CSP with mPltF, despite the putative salt bridge with D263K predicted computationally, and the increased catalytic activity observed in the mutant. We hypothesize that since helix III is more solvent accessible, and less buried in the PPI compared to D38, the salt bridge is more transient, resulting in lack of detection via CSP.

These three synergistic mutations show that the designs generated with our method successfully created an electrostatic–dependent interface to complement and attract the negatively charged surface of AcpP. The addition of electrostatic interface interactions resembles the PPIs of native AcpP FAS partner enzymes revealed from previously solved X–ray crystal structures, supporting the method's ability to design productive PPIs.[16] While this current work focuses on designing interfaces between two stand-alone proteins, many

carrier-protein dependent pathways are connected by a polypeptide linker, such as the case in Type I FAS, PKS, and NRPS systems.[11, 16] In many cases, the linker between the carrier protein and partner protein may form specific linker-protein interactions crucial for enzyme catalysis, which may be incorporated in the interface design process.[30]

CONCLUSIONS

The ability to re–engineer carrier protein–dependent pathways to create biosynthetic products has been a long sought–after goal. Here we develop an experimentally guided computational workflow, which incorporates both structure and function data to design mutations more efficiently than the current state of the art Rosetta REF15 score function.[25] We engineered a hybrid FAS/NRPS enzyme through interface mutations of an A domain from NRPS to interact with ACP from FAS. While the default Rosetta protocol generated only 3 mutants with > 50% activity and 7 false positives, refining the score function based on the experimental assay resulted in 8 mutants with greater than 50% activity and only 1 false positive. Additionally, the most active mutant identified with the refined score function was almost 10 times more catalytic than the mutant identified with the default score function. This method advances the current state of interface engineering and provides a promising strategy for harnessing control over carrier protein–dependent pathways for designing new natural products.

METHODS

Computational Methods.

The following sections provide an overview of the methods used for computationally–guided interface design studies. Rosetta version 3.9 was used for all computational designs with the REF15 score function.[25] All scripts and files necessary to reproduce Rosetta methods can be found at https://github.com/tsztain/PltF–AcpP–design.

Structure preparation.

The crystal structure of the trapped PltF • PltL complex PDB: 6O6E[13,31] was used to obtain initial coordinates for PltF. AcpP from PDB: 2FAD[32] was aligned to the PltL in PyMOL to generate an initial AcpP • PltF complex (Figure S1). PltL was then deleted and not used. The rotamer packing flags –ex1 and –ex2 were used in all cases to include additional $\chi 1$ and $\chi 2$ rotamers. First, PltF residues 449–450, which are not resolved in the crystal structure were modeled using Rosetta loop modeling. Next, the structure was relaxed using the FastRelax protocol:[https://www.rosettacommons.org/docs/latest/scripting_documentation/RosettaScripts/Movers/movers_pages/FastRelaxMover].

Interface design.

A RosettaScripts design protocol was used to generate 1,000 structures per design round. The PltF residues K402 and K486 were restricted to repacking and not designed due to their importance for catalytic activity.[13] Only residues of PltF within 8 Å of AcpP were allowed to be mutated. A favored native residue bonus of 1 was applied to avoid excessive mutations. For 1,000 iterations, the protocol first performs a local refinement stage of

full atom docking, followed by interface design, then full atom backbone and side chain minimization. Acceptance criteria for each iteration required a negative binding score and an interface solvent accessible surface area greater than 800 $Å^2$.

Analysis and score refinement.

Designs were analyzed based on sequence profile (Table S2) Mutations persisting in over 40% of the structures were prepared for *in vitro* analysis. For refinement of the REF15 Rosetta score function, individual score terms were examined to identify the score term with the highest correlation to the experimental assay. This was the electrostatic score term, which has a coefficient of 0.875 in the unmodified score function.[25] Several increased coefficients between 0.9 and 2.5 were tested, with 1.5 showing the best correlation between predicted mutation and experimental activity.

Protein Expression.

Wild–type PltF[31] or the mutant PltF plasmids were transformed into *E. coli* BL21 cells. The cells were grown in 50 mL LB media with 50 μg/mL kanamycin at 37 °C. Expression was induced with 0.5 mM IPTG at an OD600 of 0.6. The cells were grown at 16 °C for 16 h then harvested at 4000 relative centrifugal force (RCF). The cells were resuspended in 1.4 mL of 50 mM NaCl, 50 mM Tris pH 7.5, and 1× BugBuster Protein Extraction Reagent (70921–3, Millipore Sigma) and incubated for 20 min at room temperature and shaking at 500 rpm. The lysate was centrifuged at 12000 RCF at 12 °C for 45 min and the supernatant was passed through 0.15 mL bed volume of Novagen Ni–NTA resin. The column was then washed with 2 mL of 50 mM NaCl, 50 mM Tris pH 7.50 and then 2 mL of the same buffer with 20 mM imidazole. PltF was eluted with 0.25 mL of 50 mM NaCl, 50 mM Tris pH 7.5, and 250-mM imidazole, then dialyzed using Slide–A–Lyzer Dialysis Cassettes (Pierce, 66383) overnight into 50 mM NaCl, 50 mM Tris pH 7.5, 10% glycerol at 4 °C.

Preparation of holo–AcpP.

holo–AcpP was prepared by co–transforming C–terminal His–tagged AcpP from *E. coli*[3] and Sfp from *Bacillus subtilis*[33] into *E. coli* BL21 cells. The cells were grown in LB broth with 50 μg/mL kanamycin and 100 μg/mL ampicillin at 37 °C and induced with 0.5 mM IPTG at an OD_{600} of 0.6. The cells were then grown for 4 h at 37 °C then harvested at 2500 relative centrifugal force. The cells were resuspended in 50 mM NaCl, 50 mM Tris pH 7.5 and lysed using an Ultrasonic Processor FS–600N (4 s off, 1 s on for 10 min) on ice. The lysate was centrifuged at 12000 RCF at 4 °C for 45 min and the supernatant was passed through 2 mL bed volume of Novagen Ni–NTA resin. The column was washed with 50 mL of buffer and AcpP was eluted as described for the PltF purification. Passing of the nickel pure AcpP sample through an Ascentis C18 column on an Agilent 1100 HPLC using a gradient of increasing CH_3CN, starting at 25% aq. CH_3CN and increasing until 95% aq. CH_3CN, revealed 90% *holo*–AcpP, with the remaining 10% being *apo*–AcpP. All solvents for HPLC contained 0.05% trifluoroacetic acid. Full holofication was achieved by incubating the *apo*/*holo* mixture with 0.004 mM Sfp, 50 mM Tris pH 7.5, 12.5 mM $MgCl_2$, 1 mM TCEP, 0.5 mM CoA, and 150 mM NaCl overnight at 37 °C. The reaction was dialyzed into 50 mM Tris pH 7.50 and run through a HiTrapQ HP 5 mL (Cytiva, 17115401) column for pure *holo*–AcpP.

PltF Mutagenesis.

The PltF point mutations were introduced *via* QuikChange PCR.[34] The primer sequences are listed in Table S5.

PltF activity assays.

Initial mPltF activity assays were performed by incubating 10 μM mPltF, 15 μM *holo*–AcpP, 50 mM Tris pH 7.50, 12.5 mM $MgCl_2$, 2 mM TCEP, 5 mM ATP, and 5 mM L–proline for 2 h at 25 °C. The reaction was quenched with 2% formic acid and centrifuged for 10 min, 10k rpm, at 4 °C. The supernatant was passed through an Ascentis C18 column on an Agilent 1100 HPLC, starting with 25% aq. CH_3CN for 2 min, then increasing to 56% aq. CH_3CN over 13 min, then increasing to 95% aq. CH_3CN over 3 min, and finally decreased to 25% aq. CH_3CN over 5 min. Absorbance at 210 nm was used for integration of the *holo*–AcpP and prolyl–AcpP peaks, which eluted at 11.4 min and 11.1 min, respectively. Percent prolyl–AcpP was calculated by dividing the integrated prolyl–AcpP peak by the summation of the integrated prolyl– and *holo*–AcpP peaks. Each assay was performed in triplicate.

mPltF Time Course Studies.

Time course experiments of mPltF were performed by incubating 1.01 μM mPltF with 45 μM *holo*–AcpP, 50 mM Tris pH 7.5, 12.5 mM $MgCl_2$, 2 mM TCEP, 5 mM ATP, and 5 mM L–proline for 90 min, where an aliquot of each reaction was quenched with 2% formic acid at a 15 min interval. The quenched reactions were analyzed through HPLC as described previously. The linear portion of the time course experiments was used to calculate the turnover rate. Each time–course experiment was performed in duplicate. The exception is the WT PltF activity for AcpP, where the turnover rate was estimated from the initial activity assay described above due to very low prolylation activity.

General Methods for the Synthesis of Desulfopantetheine (1).

All reagents were purchased from Sigma–Aldrich or Fisher Scientific and used without further purification. Solvents were purchased from Fisher Scientific. All synthetic operations were carried out under an argon atmosphere. Deuterated NMR solvents were obtained from Cambridge Isotope Laboratories. ^1H NMR and ^{13}C NMR spectra were recorded on a Bruker AVA300 operating at 300 MHz for ^1H and 75 MHz for ^{13}C, a JEOL 400 400 MHz for ^1H and 100 MHz for ^{13}C or a JEOL 500 MHz for ^1H and 125 MHz for ^{13}C spectrometers. Chemical shift δ values for ^1H and ^{13}C spectra are reported in parts per million (ppm) and multiplicities are abbreviated as s = singlet, d = doublet, t = triplet, q = quartet, m = multiplet, br = broad. ^{13}C NMR spectra were recorded with proton decoupling. Raw FID data was processed using MestreNova 12.0.3. Electrospray (ESI) mass spectrometric analyses were performed using a ThermoFinnigan LCQ Deca spectrometer. A Thermo Scientific LTQ Orbitrap XL mass spectrometer was used for high–resolution electrospray ionization mass spectrometry analysis (HR–ESI–MS). Mass spectral analysis was conducted through the Molecular Mass Spectrometry Facility at UC San Diego.

3–((4*R*)–5,5–dimethyl–2–phenyl–1,3–dioxane–4–carboxamido)propanoic acid (2).

Concentrated sulfuric acid (2.2 mL) was added to a suspension of calcium D–pantethenoate (5.0 g, 21.0 mmol) in DMF (100 mL). After stirring at rt for 1 h, 10–camphorsulfonic (235 mg, 1.05 mmol, 0.05 eq) and benzaldehyde dimethyl acetal (6.58 mL, 42.0 mmol, 2 eq) were added sequentially. Stirring continued overnight at rt. At completion the reaction mixture was partitioned with 1 volume of EtOAc/H_2O 3 times. The combined organic extracts were washed with 1 volume of 50% saturated brine, water, and brine sequentially to remove the DMF. The organic layer was dried over Na_2SO_4 and evaporated to yield a wet crystalline mass. This was washed with cold (−20° C) DCM and collected by filtration to yield 3.46 g (53% yield) of acid **2** as white crystalline material. ^{1}H NMR (400 MHz, $CDCl_3$) δ 7.48 (dd, *J* = 7.5, 2.0 Hz, 2H), 7.39 (m, 3H), 7.08 (s, 1H), 5.49 (s, 1H), 4.12 (s, 1H), 3.72 (d, *J* = 11.4 Hz, 1H), 3.66 (d, *J* = 11.2 Hz, 1H), 3.57 (dq, *J* = 12.3, 6.1 Hz, 1H), 3.49 (dq, *J* = 13.9, 6.3 Hz, 1H), 2.59 (t, , *J* = 6.3 Hz, 2H), 1.10 (s, 3H), 1.09 (s, 3H); ^{13}C NMR (100 MHz, $CDCl_3$) δ 177.1, 169.6, 137.8, 129.3, 128.5, 126.2, 101.4, 83.8, 78.6, 34.2, 33.9, 33.3, 21.9, 19.2; HRMS (ES–ESI–TOFMS) *m/z* calcd. for $C_{16}H_{21}O_5NNa$ $[M+Na]^+$: 330.1312, found 330.1313.

(4*R*)–*N*–(3–(ethylamino)–3–oxopropyl)–5,5–dimethyl–2–phenyl–1,3–dioxane–4–carboxamide (3).

DIPEA (81 mg, 0.63 mmol, 2.0 eq), ethylamine • HCl (51 mg, 0.38 mmol, 1.2 eq), HOBt (51 mg, 0.38 mmol, 1.2 eq), and EDCI (72 mg, 0.38 mmol, 1.2 eq) were added sequentially to acid **S1** (96 mg, 0.31 mmol) in CH_2Cl_2 (1.6 mL). After stirring overnight at rt, the reaction was diluted with CH_2Cl_2 (3 mL) and quenched satd. aqueous NH_4Cl (5 mL). The organic layer was separated and the aqueous was extracted CH_2Cl_2 (3 mL). The combined organic fractions were washed with satd. $NaHCO_3$ (5 mL) and brine (5 mL). The combined organic phases were dried over Na_2SO_4, filtered, and concentrated on a rotary evaporator. Pure amide **3** (193 mg, 99%) was obtained as a colorless oil by flash chromatography, eluting with a gradient of CH_2Cl_2 to 1:18 CH_2Cl_2/MeOH. ^{1}H NMR (300 MHz, $CDCl_3$) δ 7.50 (m, 2H), 7.39 (m, 3H), 7.03 (m, 1H), 5.95 (m, 1H), 5.50 (s, 1H), 4.09 (s, 1H), 3.73 (d, *J* = 11.4 Hz, 1H), 3.67 (d, *J* = 11.9 Hz, 1H), 3.54 (m, 2H), 3.27 (dd, *J* = 7.3, 5.5 Hz, 2H), 3.22 (dd, *J* = 7.3, 5.5 Hz, 2H), 2.40 (t, *J* = 6.2 Hz, 2H), 1.10 (s, 3H), 1.10 (s, 3H), 1.09 (t, *J* = 7.3 Hz, 3H); ^{13}C NMR (75 MHz, $CDCl_3$) δ 170.6, 169.6, 137.7, 129.4, 128.5, 126.3, 101.6, 84.0, 78.6, 77.4, 36.3, 35.1, 34.5, 33.3, 22.0, 19.3, 14.9; HRMS (ES–ESI–TOFMS) *m/z* calcd. for $C_{18}H_{26}O_4N_2Na$ $[M+Na]^+$: 357.1785, found 357.1789.

Desulfopantetheine (1).

Intermediate **3** (33 mg, 0.098 mmol) was dissolved in EtOAc (1 mL). Solid 10% Pd/C (5 mg) was added. The atmosphere within the flask was changed to H_2 by three repetitions of degassing by vacuum and charging with H_2. The resulting suspension was stirred overnight at rt. After TLC indicated complete deprotection the solution was filtered over a bed of Celite, and the filtrate evaporated to yield 20 mg of **1** (82%) as an oil. ^{1}H NMR (500 MHz, CD_3OD) δ 3.88 (s, 1H), 3.48 (m, 2H), 3.47 (d, *J* = 10.9 Hz, 1H), 3.38 (d, *J* = 11.0 Hz, 1H), 3.20 (dd, *J* = 7.3, 1.1 Hz, 1H), 3.17 (dd, *J* = 7.3, 1.1 Hz, 1H), 2.40 (t, *J* = 6.7 Hz, 2H), 1.10 (t, *J* = 7.3 Hz, 3H), 0.91 (s, 3H), 0.91 (s, 3H); ^{13}C NMR (125 MHz, CD_3OD) δ 176.1, 173.5,

77.1, 70.3 40.4, 36.4, 36.4, 35.2, 21.3, 20.8, 14.7; HRMS (ES–ESI–TOFMS) *m/z* calcd. for $C_{11}H_{22}N_2O_4Na$ $[M+Na]^+$: 269.1472, found 269.1470.

Growth, expression, and purification of ^{15}N–AcpP.—*Escherichia coli* AcpP with a C–terminal His_6 tag in a pET–22b vector transformed into BL21 cells[3] was grown overnight in LB media (5 mL) with 100 μg/mL ampicillin at 37 °C. Cells were washed twice with sterile H_2O to remove LB and resuspended in 1 L of a minimal media with 1 g ^{15}N–NH_4Cl (Cambridge Isotopes laboratory) as the only nitrogen source, to achieve uniform ^{15}N labeling. The media also consisted of 6 g Na_2HPO_4, 3 g KH_2PO_4, 0.5 g NaCl, 100 mg ampicillin, 0.25 g $MgSO_4 \cdot 7H_2O$, 0.015 g $CaCl_2 \cdot 2H_2O$, 0.01 g thiamine, 0.003 g $FeSO_4 \cdot 7H_2O$, and 4 g D–glucose. Cells were grown at 37 °C until reaching an OD_{600} between 0.6 to 1.0 before induction of protein expression with 0.5 mM IPTG, then continued at 37 °C overnight. Cells were collected by centrifugation and lysed by sonication in a buffer consisting of 150 mM NaCl, 50 mM phosphate pH 7.5, 10% glycerol, with lysozyme and DNase. Lysate was clarified by centrifugation followed by standard nickel purification using Ni–NTA resin (ThermoFisher Scientific).

Preparation of desulfo–AcpP.—Desulfo–AcpP was prepared from Ni^{2+} affinity purified AcpP, which consists of a mixture of both *apo*- and *holo*-AcpP populations. All of the AcpP was converted to *apo*–AcpP with 1 μM AcpH in 50 mM Tris pH 7.4, 150 mM NaCl, 10% glycerol,5 mM $MgCl_2$, 0.5 mM $MnCl_2$, and 0.1% TCEP. After reaction for 4 h at 37 °C, completion was confirmed using conformationally sensitive Urea-PAGE. AcpH was removed through FPLC purification with a Superdex 75 column. Loading of the desulfopantetheine group to *apo*-AcpP was carried out using the one-pot chemoenzymatic method.[35] Reactions contained 1 mg/mL AcpP, 12.5 mM $MgCl_2$, 10 mM ATP, 0.1 μM CoaA, 0.1 μM CoaD, 0.1 μM CoaE, 0.2 μM *B. Subtilis* Sfp 0.01% azide, 0.1% TCEP, and 0.1 mM desulfopantetheine (**1**) and were run overnight at 37 °C. The concentrated protein was purified by size exclusion chromatography on a Superdex 75 column into NMR buffer containing: 10 mM potassium phosphate pH 7.4, 0.5 mM TCEP, and 0.1% sodium azide.

NMR titration studies.—All experiments were performed at the UCSD Biomolecular NMR facility on a Avance 800MHz (Bruker) spectrometer. ^1H-^{15}N HSQC experiments were performed at 37 °C, with a 1.5 s recycle delta and 2048 data points. Assignments were made from overlay with previous backbone HSQC assignments of *holo*–AcpP. It was observed that the change from *holo* to "desulfo–*holo*" had minimal effects on the spectra of AcpP. Chemical shift perturbation values were calculated using an α value of 0.2 with the formula:

$$CSP = \sqrt{\frac{1}{2}[\delta_H^2 + (\alpha \cdot \delta_N)^2]}$$

Titrations were performed at the concentrations described for each experiment as described in the manuscript text. HSQCs were performed with a 1.5 s recycle delta and 2048 data points. Processing and visualization were performed with TOPSPIN and the POKY software suite.[36]

Electrostatic potential calculation.—The ABPS program[37] in PyMOL was used to calculate the electrostatic surface potentials of the relaxed protein model outputs from the RosettaScripts design using the default parameters.

Interface analysis.—Protein Interfaces, Surfaces, and Assemblies (PISA) [https://www.ebi.ac.uk/pdbe/pisa/] from the European Bioinformatics Institute was used to identify the residues involved in the AcpP • PltF and AcpP • PltF Q438R D263K A230R interface models.

PyMOL mutagenesis.—The Mutagenesis Wizard in PyMOL was used to mutate, fit, and visualize the A230R mutation [https://pymolwiki.org/index.php/Mutagenesis]. The rotamer was chosen based on a low clash score and proximity to the PPant arm.

Supplementary Material

Refer to Web version on PubMed Central for supplementary material.

ACKNOWLEDGEMENTS

This work was supported by NIH R01 GM095970. T.S. is an NSF Graduate Research Fellowship Program recipient under Grant DGE–1650112. J.C.C. is supported by NIH T32 GM008326 and NIH F31 GM137616. G.W.H. is supported by NIH K12HL141956.

ABBREVIATIONS

A	Adenylation domain
AMP	Adenosine monophosphate
DH	dehydratase
FAS	Fatty acid synthase
ER	enoyl reductase
KR	ketoreductase
NRPS	non–ribosomal peptide synthetase
NMR	nuclear magnetic resonance
PPant	phosphopantetheine
PKS	polyketide synthase
PPIs	protein–protein interactions

REFERENCES

(1). Sztain T; Bartholow TG; Lee DJ; Casalino L; Mitchell A; Young MA; Wang J; McCammon JA; Burkart MD Decoding Allosteric Regulation by the Acyl Carrier Protein. Proc. Natl. Acad. Sci. USA 2021, 118, e2025597118. [PubMed: 33846262]

(2). Bartholow TG; Sztain T; Patel A; Lee DJ; Young MA; Abagyan R; Burkart MD Elucidation of Transient Protein–Protein Interactions within Carrier Protein–Dependent Biosynthesis. Commun. Biol 2021, 4, 340. [PubMed: 33727677]

(3). Brown AS; Calcott MJ; Owen JG; Ackerley DF Structural, functional and evolutionary perspectives on effective re-engineering of non-ribosomal peptide synthetase assembly lines. Nat. Prod. Rep 2018, 35, 1210–1228. [PubMed: 30069573]

(4). Gulick AM, Aldrich CC Trapping interactions between catalytic domains and carrier proteins of modular biosynthetic enzymes with chemical probes. Nat. Prod. Rep 2018, 35, 1156–1184. [PubMed: 30046790]

(5). Nguyen C; Haushalter RW; Lee DJ; Markwick PRL; Bruegger J; Caldara–Festin G; Finzel K; Jackson DR; Ishikawa F; O'Dowd B; McCammon JA; Opella SJ; Tsai S–C; Burkart MD Trapping the Dynamic Acyl Carrier Protein in Fatty Acid Biosynthesis. Nature 2014, 505, 427–431. [PubMed: 24362570]

(6). Milligan JC; Lee DJ; Jackson DR; Schaub AJ; Beld J; Barajas JF; Hale JJ; Luo R; Burkart MD; Tsai S–C Molecular Basis for Interactions between an Acyl Carrier Protein and a Ketosynthase. Nat. Chem. Biol 2019, 15, 669–671. [PubMed: 31209348]

(7). Dodge GJ; Patel A; Jaremko KL; McCammon JA; Smith JL; Burkart MD Structural and Dynamical Rationale for Fatty Acid Unsaturation in *Escherichia coli*. Proc. Natl. Acad. Sci. USA 2019, 116, 6775–6783. [PubMed: 30872475]

(8). Mindrebo JT; Patel A; Kim WE; Davis TD; Chen A; Bartholow TG; La Clair JJ; McCammon JA; Noel JP; Burkart MD Gating Mechanism of Elongating β–Ketoacyl–ACP Synthases. Nat. Commun 2020, 11, 1727. [PubMed: 32265440]

(9). Lou JW; Iyer KR; Hasan SMN; Cowen LE; Mazhab–Jafari MT Electron Cryomicroscopy Observation of Acyl Carrier Protein Translocation in Type I Fungal Fatty Acid Synthase. Sci. Rep 2019, 9, 12987. [PubMed: 31506493]

(10). Sarria S; Bartholow TG; Verga A; Burkart MD; Peralta–Yahya P Matching Protein Interfaces for Improved Medium–Chain Fatty Acid Production. ACS Synth. Biol 2018, 7, 1179–1187. [PubMed: 29722970]

(11). Jaremko MJ; Davis TD; Corpuz JC; Burkart MD Type II Non–Ribosomal Peptide Synthetase Proteins: Structure, Mechanism, and Protein–Protein Interactions. Nat. Prod. Rep 2020, 37, 355–379. [PubMed: 31593192]

(12). Jaremko MJ; Lee DJ; Patel A; Winslow V; Opella SJ; McCammon JA; Burkart MD Manipulating Protein–Protein Interactions in Nonribosomal Peptide Synthetase Type II Peptidyl Carrier Proteins. Biochemistry 2017, 56, 5269–5273. [PubMed: 28920687]

(13). Corpuz JC; Podust LM; Davis TD; Jaremko MJ; Burkart MD Dynamic Visualization of Type II Peptidyl Carrier Protein Recognition in Pyoluteorin Biosynthesis. RSC Chem. Biol 2020, 1, 8–12. [PubMed: 33305272]

(14). Campbell JW; Cronan JE Bacterial Fatty Acid Biosynthesis: Targets for Antibacterial Drug Discovery. Annu. Rev. Microbiol 2001, 55, 305–332. [PubMed: 11544358]

(15). Janßen H; Steinbüchel A Fatty Acid Synthesis in *Escherichia coli* and Its Applications towards the Production of Fatty Acid Based Biofuels. Biotechnol. Biofuels 2014, 7, 7. [PubMed: 24405789]

(16). Chen A; Re RN; Burkart MD Type II Fatty Acid and Polyketide Synthases: Deciphering Protein–Protein and Protein–Substrate Interactions. Nat. Prod. Rep 2018, 35, 1029–1045. [PubMed: 30046786]

(17). Magnuson K; Jackowski S; Rock CO; Cronan JE Regulation of Fatty Acid Biosynthesis in *Escherichia coli*. Microbiol. Rev 1993, 57, 522–542. [PubMed: 8246839]

(18). Lin S; Cronan JE Closing in on Complete Pathways of Biotin Biosynthesis. Mol. BioSyst 2011, 7, 1811–1821. [PubMed: 21437340]

(19). Beld J; Finzel K; Burkart MD Versatility of Acyl–Acyl Carrier Protein Synthetases. Chem. Biol 2014, 21, 1293–1299. [PubMed: 25308274]

(20). Metzger JO Fats and Oils as Renewable Feedstock for Chemistry. Eur. J. Lipid Sci. Technol 2009, 111, 865–876

(21). Biermann U; Bornscheuer U; Meier MAR; Metzger JO; Schäfer HJ Oils and Fats as Renewable Raw Materials in Chemistry. Angew. Chem. Int. Ed 2011, 50, 3854–3871.

(22). Groweiss A; Cardellina JH; Pannell LK; Uyakul D; Kashman Y; Boyd MR Novel Cytotoxic, Alkylated Hydroquinones from *Lannea Welwitschii*. J. Nat. Prod 1997, 60, 116–121. [PubMed: 9051911]

(23). Bru mLey D; Spencer KA; Gunasekera SP; Sauvage T; Biggs J; Paul VJ; Luesch H Isolation and Characterization of Anaephenes A–C, Alkylphenols from a Filamentous Cyanobacterium (*Hormoscilla* sp., *Oscillatoriales*). J. Nat. Prod 2018, 81, 2716–2721. [PubMed: 30489078]

(24). Fleishman SJ; Leaver–Fay A; Corn JE; Strauch E–M; Khare SD; Koga N; Ashworth J; Murphy P; Richter F; Lemmon G; Meiler J; Baker D RosettaScripts: A Scripting Language Interface to the Rosetta Macromolecular Modeling Suite. PLoS ONE 2011, 6, e20161. [PubMed: 21731610]

(25). Alford RF; Leaver–Fay A; Jeliazkov JR; O'Meara MJ; DiMaio FP; Park H; Shapovalov MV; Renfrew PD; Mulligan VK; Kappel K; Labonte JW; Pacella MS; Bonneau R; Bradley P; Dunbrack RL; Das R; Baker D; Kuhlman B; Kortemme T; Gray JJ The Rosetta All–Atom Energy Function for Macromolecular Modeling and Design. J. Chem. Theory Comput 2017, 13, 3031–3048. [PubMed: 28430426]

(26). Stranges PB; Kuhlman B A Comparison of Successful and Failed Protein Interface Designs Highlights the Challenges of Designing Buried Hydrogen Bonds. Protein Sci. 2013, 22, 74–82. [PubMed: 23139141]

(27). Byers DM; Gong H Acyl Carrier Protein: Structure–Function Relationships in a Conserved Multifunctional Protein Family. Biochem. Cell Biol 2007, 85, 649–662. [PubMed: 18059524]

(28). Thomas MG; Burkart MD; Walsh CT Conversion of L–Proline to Pyrrolyl–2–Carboxyl–S–PCP during Undecylprodigiosin and Pyoluteorin Biosynthesis. Chem. Biol 2002, 9, 171–184. [PubMed: 11880032]

(29). Zhou H–X; Pang X Electrostatic Interactions in Protein Structure, Folding, Binding, and Condensation. Chem. Rev 2018, 118, 1691–1741. [PubMed: 29319301]

(30). Izoré T; Cryle MJ. The many faces and important roles of protein-protein interactions during non-ribosomal peptide synthesis, Nat. Prod. Rep 2018, 35, 1120–1139. [PubMed: 30207358]

(31). Corpuz JC; Patel A; Davis TD; Podust LM; McCammon JA; Burkart MD Essential Role of Loop Dynamics in Type II NRPS Biomolecular Recognition. ACS Chem. Biol 2022, 17, 2890–2898. [PubMed: 36173802]

(32). Roujeinikova A; Simon WJ; Gilroy J; Rice DW; Rafferty JB; Slabas AR; Structural studies of fatty acyl–(acyl carrier protein) thioesters reveal a hydrophobic binding cavity that can expand to fit longer substrates. J. Mol. Biol 2007, 365, 135–145. [PubMed: 17059829]

(33). Quadri LE, Weinreb PH, Lei M, Nakano MM, Zuber P, Walsh CT. Characterization of Sfp, a *Bacillus subtilis* phosphopantetheinyl transferase for peptidyl carrier protein domains in peptide synthetases Biochemistry. 1998, 37, 1585–1595. [PubMed: 9484229]

(34). Xia Y; Xun L Methods Revised Mechanism, and Improved Efficiency of the QuikChange Site–Directed Mutagenesis Method. Mol. Biol 2017, 1498, 367–374.

(35). Worthington AS; Burkart MD One-pot chemo-enzymatic synthesis of reporter-modified proteins. Org. Biomol. Chem 2006, 4, 44–46. [PubMed: 16357994]

(36). Lee W; Rahimi M; Lee Y; Chiu A POKY: a software suite for multidimensional NMR and 3D structure calculation of biomolecules. Bioinformatics. 2021, 37, 3041–3042. [PubMed: 33715003]

(37). Jurrus E; Engel D; Star K; Monson K; Brandi J; Felberg LE; Brookes DH; Wilson L; Chen J; Liles K; Chun M; Li P; Gohara DW; Dolinsky T; Konecny R; Koes DR; Nielsen JE; Head–Gordon T; Geng W; Krasny R; Wei GW; Holst MJ; McCammon JA; Baker NA Improvements to the APBS biomolecular solvation software suite. Protein Sci. 2018, 27, 112–128. [PubMed: 28836357]

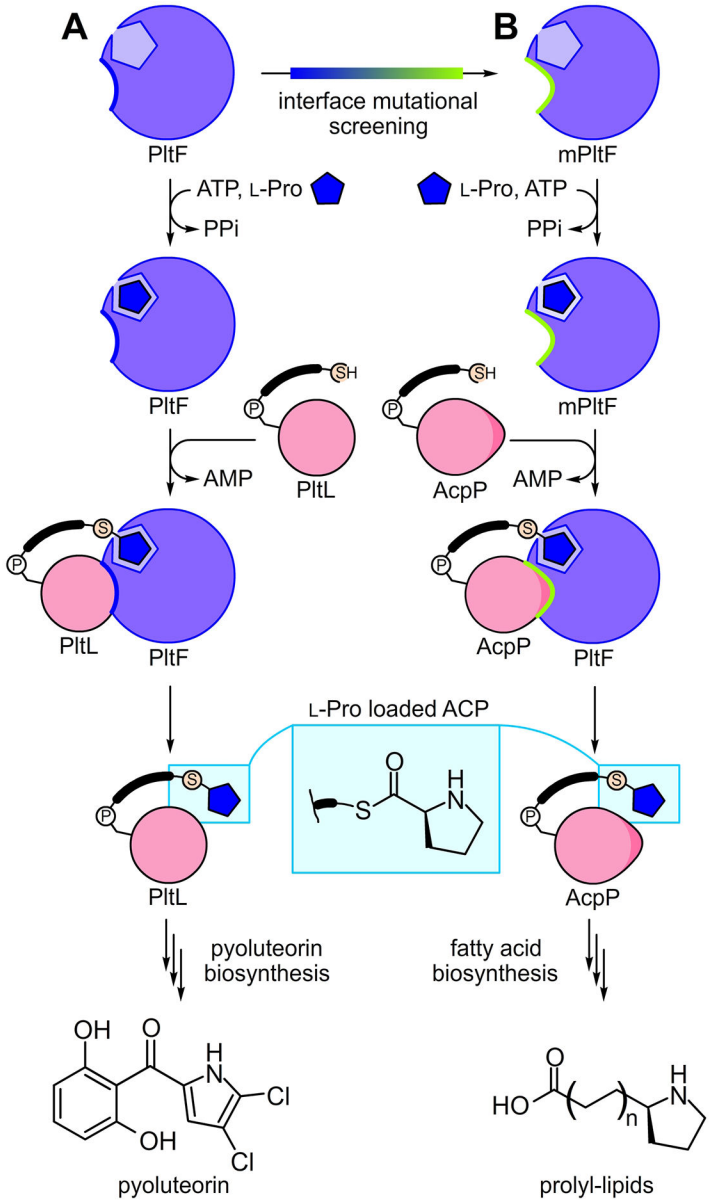

Figure 1.

Adenylation and thiolation reactions by PltF. **A)** Wild type reaction of PltF. PltF adenylates proline to create a prolyl–AMP intermediate (blue square), then transfers the prolyl moiety to *holo*–PltL. The pyrrolidine group is passed off and incorporated into pyoluteorin. **B)** Designed PltF reaction. The interface mutant PltF (mPltF) instead transfers ATP–activated proline to *holo*–AcpP. Prolyl–AcpP then shuttles the pyrrolidine group through the *E. coli* FAS for carbon chain elongation of the product to produce a target class of prolyl–lipids. **(1 column)**

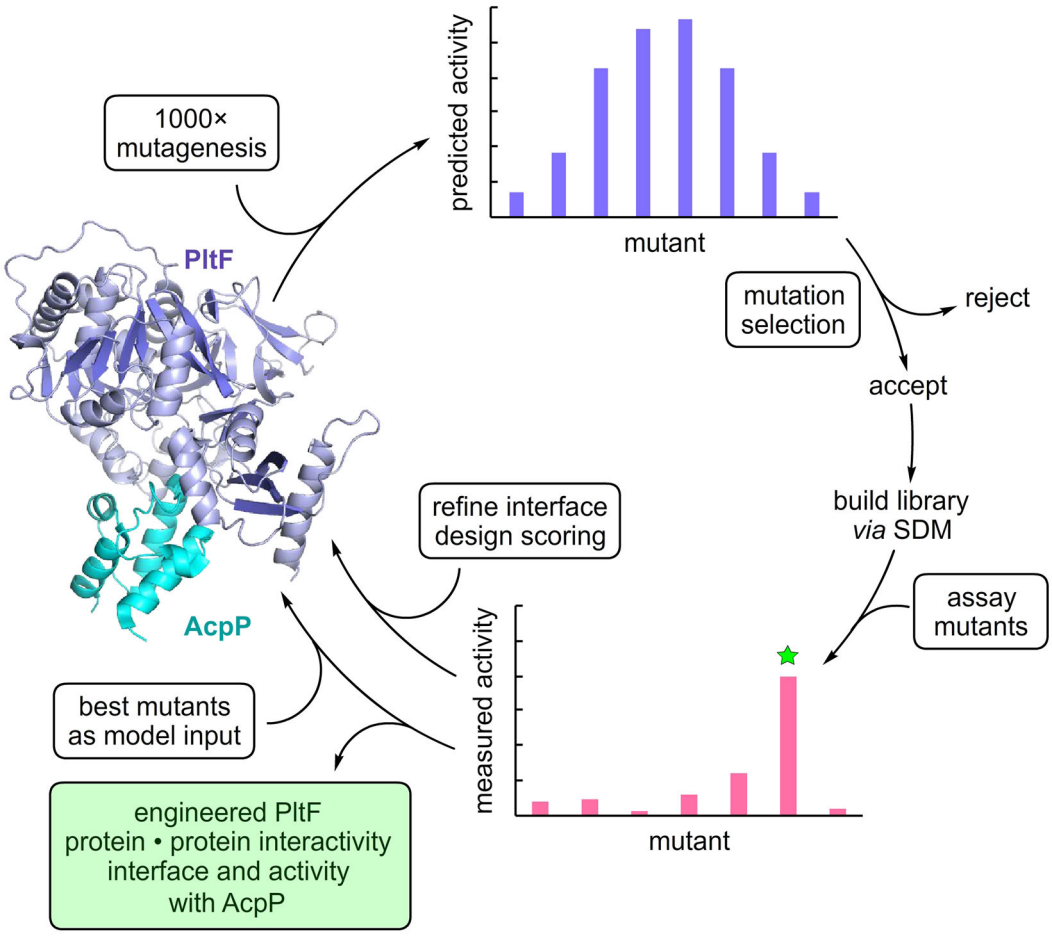

Figure 2.

Schematic of computational and experimental interface design workflow. An initial interface with PltF (purple) is generated through carrier protein superposition of AcpP (cyan) onto PltL (pink). Next, the structures are prepared by modeling missing loops, and performing relaxation. Residue or design restraints are selected followed by random mutagenesis (red) of the interface to produce 1000 mutants, which pass the score threshold. Mutants that significantly persist throughout the mutagenesis were selected for *in vitro* assay. Information from the experimental assay is then used to refine the Rosetta score function. **(1 column)**

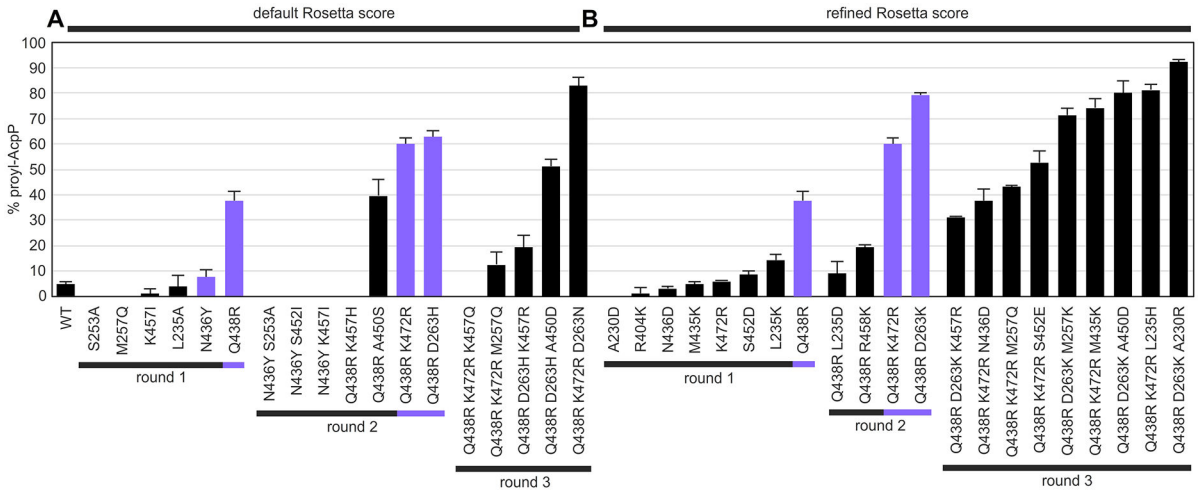

Figure 3.

Prolylation activity of designed PltF mutants. PltF activity was monitored through HPLC chromatogram peak integration after incubation of 0.010 mM mPltF with 0.015 mM *holo*–AcpP, 5 mM ATP, 12.5 mM $MgCl_2$, and 5 mM L–proline for 2 h at 25° C. The **A)** default or **B)** refined score function was used to identify mutants through iterative rounds of Rosetta interface design. Lavender bars denote mutations used for the next round of screening. **(2 columns)**

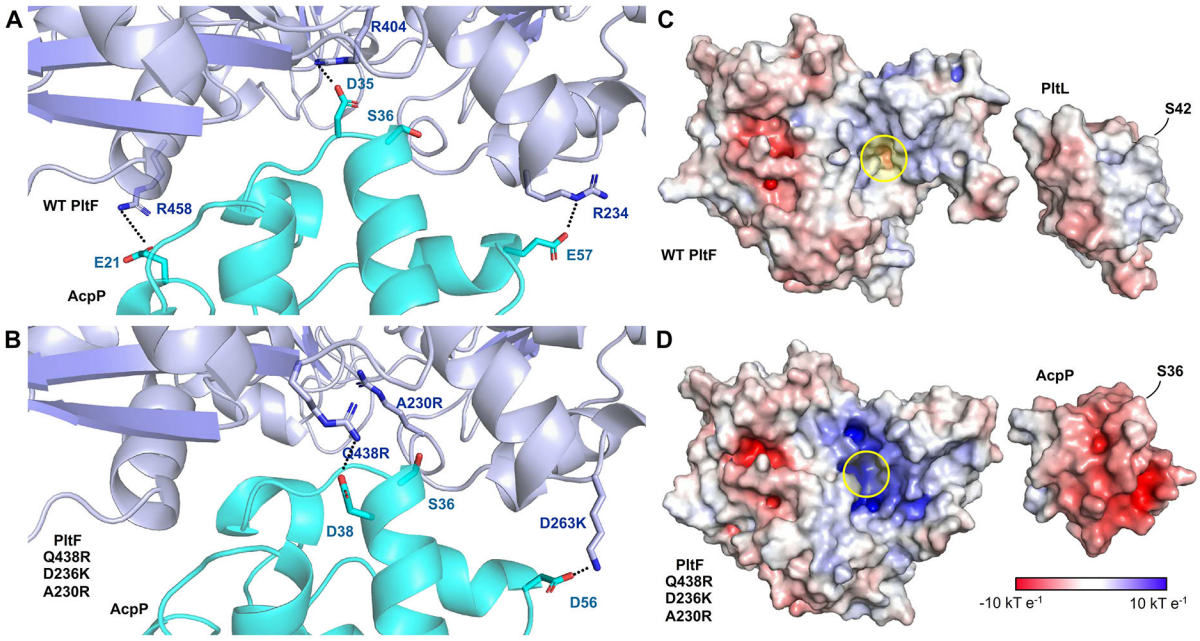

Figure 4.

Comparison of WT and designed protein–protein interfaces. The predicted salt bridge interactions at the interface of the relaxed model of WT PltF docked to **A)** AcpP and **B)** the Rosetta model of PltF Q438R D263K A230R bound to AcpP. **C)** Electrostatic potentials mapped onto the surface of PltL (PDB ID: 2N5H) and PltF (PDB ID: 6O6E). **D)** Electrostatic potentials mapped onto the surface of AcpP (PDB ID: 2FAD) and a Rosetta model of PltF Q438R D263K A230R. Circled in yellow is the entrance to the PPant tunnel. **(2 columns)**

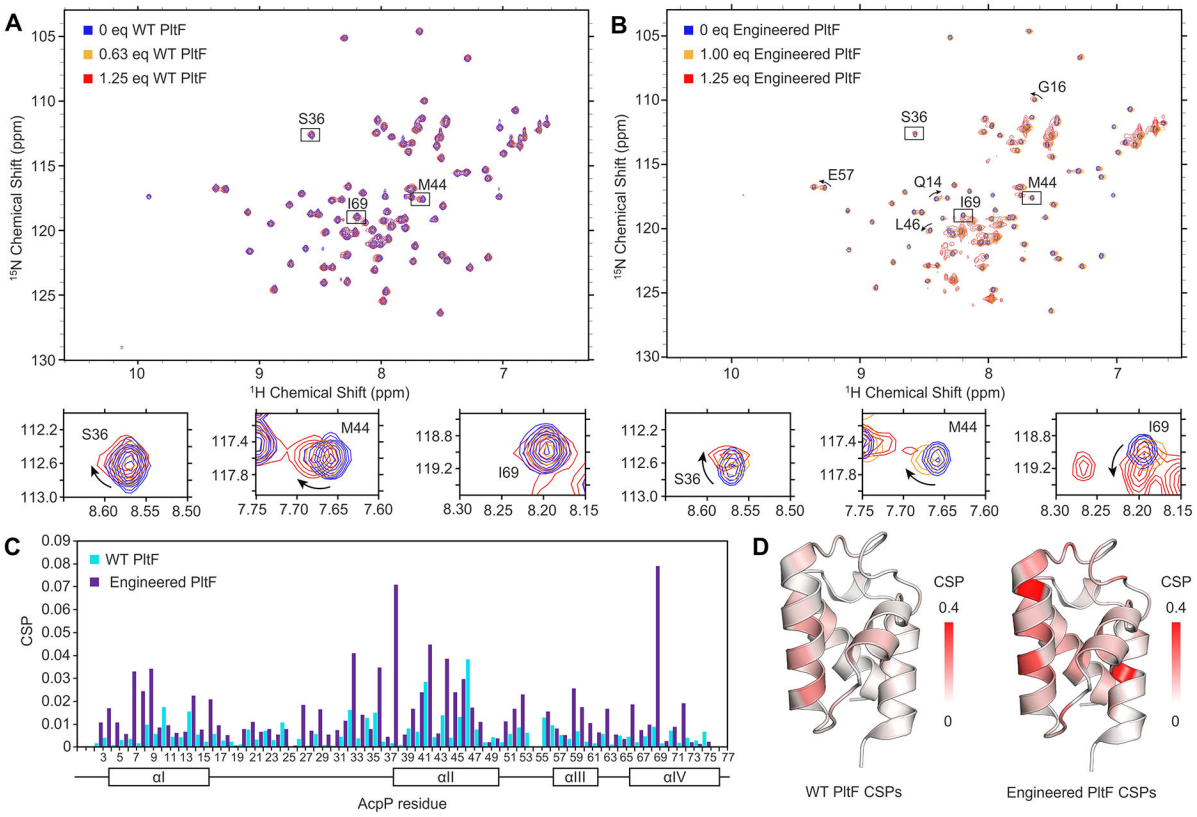

Figure 5.

NMR titrations of PltF and AcpP. $^{1}H–^{15}N$ HSQC spectra of desulfo–AcpP titrated with **A**) WT PltF and **B**) the engineered triple mutant PltF. Enlarged view of select residues perturbed in are provided under each plot. **C**) CSP plot of WT and triple mutant PltF calculated from **A**) and **B**). **D**) Structures of AcpP colored by CSP in WT titration and colored by CSP in the engineered triple mutant titration. **(2 columns)**